Published in final edited form as:

Nat Chem Biol. 2017 January ; 13(1): 62–68. doi:10.1038/nchembio.2231.

Inhibition of RAS function through targeting an allosteric regulatory site

Russell Spencer-Smith[1,2,3], **Akiko Koide**[4,5,6], **Yong Zhou**[7], **Raphael R. Eguchi**[4], **Fern Sha**[4], **Priyanka Gajwani**[1,2], **Dianicha Santana**[1,2], **Ankit Gupta**[4,5], **Miranda Jacobs**[1,2], **Erika Herrero-Garcia**[1,2,3], **Jacqueline Cobbert**[1,2], **Hugo Lavoie**[8], **Matthew Smith**[9], **Thanashan Rajakulendran**[10,11], **Evan Dowdell**[4], **Mustafa Nazir Okur**[1,2], **Irina Dementieva**[4], **Frank Sicheri**[10,11], **Marc Therrien**[8], **John F. Hancock**[7], **Mitsuhiko Ikura**[9], **Shohei Koide**[4,5,1,2,*], and **John P. O'Bryan**[1,2,3,*]

[1]Department of Pharmacology, University of Illinois at Chicago, Chicago, IL 60623, USA

[2]University of Illinois Cancer Center, University of Illinois at Chicago, Chicago, IL 60623, USA

[3]Jesse Brown VA Medical Center, Chicago, IL 60612, USA

[4]Department of Biochemistry and Molecular Biology, The University of Chicago, Chicago, IL 60637, USA

[5]Perlmutter Cancer Center, New York University Langone Medical Center, New York, NY 10016, USA

[6]Department of Medicine, New York University Langone Medical Center, New York, NY 10016, USA

[7]Department of Integrative Biology and Pharmacology, University of Texas Medical School at Houston, Houston, TX 77030, USA

[8]Institute for Research in Immunology and Cancer, Department of Pathology and Cell Biology, Université de Montréal, Montreal, Quebec, H3C 3J7 Canada

[9]Department of Medical Biophysics, Campbell Family Cancer Research Institute, Princess Margaret Cancer Centre, University of Toronto, Toronto, ON, M5G 2M9 Canada

Correspondence and requests for materials should be addressed to S.K. (Shohei.Koide@nyumc.org) and J.P.O. (obryanj@uic.edu).

PDB accession code Atomic coordinates for the NS1:RAS structure have been deposited in the Protein Data Bank with the accession code 5E95.

Supplementary information is available in the online version of the paper.

Author Contributions R.S.S, A.K., F.Sicheri, M.I., J.H., M.T., S.K., J.P.O. designed the study; M.N.O. and I.D. prepared protein for monobody isolation; A.K. and E.D. performed library selection and identified NS1; I.D. M.S. and M.I. performed and interpreted NMR experiments; T.R. and F.Sicheri analyzed RAS structures in the PDB; R.S.S. A.K, E.H.G., D.S., P.G., J.C., M.J., and M.N.O. performed biochemical and cell biology experiments; R.R.E, F.Sha., A.G., and S.K, determined X-ray structure of monobody: RAS complex; Y.Z and J.F.H. performed the nanoclustering analysis; H.L and M.T performed the BRET analysis; R.S.S, F.Sicheri., S.K. and J.P.O wrote the manuscript and all authors commented and approved the manuscript.

Competing financial interests All other authors declare no competing financial interests.

Author information Any supplementary information, chemical compound information and source data are available in the online version of the paper.

[10]Centre for Systems Biology, Lunenfeld-Tanenbaum Research Institute, Toronto, Ontario M5G 1X5, Canada

[11]Departments of Molecular Genetics and Biochemistry, University of Toronto, Toronto, Ontario M5S 1A8, Canada

[12]Department of Biochemistry and Molecular Pharmacology, New York University Langone Medical Center, New York, NY 10016, USA

Abstract

RAS GTPases are important mediators of oncogenesis in humans. However, pharmacological inhibition of RAS has proved challenging. Here, we describe a functionally critical region of RAS located outside the effector lobe that can be targeted for inhibition. We developed a synthetic binding protein (monobody), termed NS1, that bound with high affinity to both GTP- and GDP-bound states of H- and K-RAS but not N-RAS. NS1 potently inhibited growth factor signaling and oncogenic H- and K-RAS-mediated signaling and transformation but did not block oncogenic N-RAS, BRAF or MEK1. NS1 bound the α4-β6-α5 region of RAS disrupting RAS dimerization/nanoclustering, which in turn blocked CRAF:BRAF heterodimerization and activation. These results establish the importance of the α4-β6-α5 interface in RAS-mediated signaling and define a previously unrecognized site in RAS for inhibiting RAS function.

INTRODUCTION

RAS family GTPases represent critical cell signaling nodes involved in many aspects of normal development and function including regulation of proliferation, development, cell survival, and cell motility[1,2]. However, mutations in one of the three *RAS* genes (*H*-, *K*- or *N-RAS*) are present in nearly 30% of human tumors underscoring their importance in oncogenic transformation. Indeed, some tumors such as pancreatic adenocarcinomas have an incidence of K-RAS mutations approaching nearly 90%. Furthermore, tumors lacking specific RAS mutation nevertheless frequently employ RAS activity due to mutations in upstream activators of RAS such as growth factor receptors. Thus, RAS has emerged as an important therapeutic target in human carcinogenesis.

RAS proteins cycle between active GTP-bound and inactive GDP-bound states. These two states of RAS are controlled by guanine nucleotide exchange factors (GEFs) that promote the release of GDP from RAS and subsequent uptake of GTP. The nucleotide exchange process leads to large conformational changes of the switch-1 (SW1) and switch-2 (SW2) regions in the effector lobe of RAS. Once activated, RAS signaling is terminated through the action of its intrinsic GTPase activity that is enhanced by GTPase accelerating proteins (GAPs). Given the importance of RAS in driving cellular transformation and tumorigenesis, much effort has been devoted to developing pharmacological inhibitors to RAS. Although farnesyl transferase (FTase) inhibitors appeared a promising solution to inhibit RAS *in vivo*, these inhibitors have proven ineffective against mutant K-RAS due to the inherent ability of K-RAS to undergo alternative lipid modification upon blockade of the FTase. More recent efforts have led to the identification of distinct RAS inhibitory agents. Using a disulphide-based screening approach, irreversible inhibitors specific to the K-RAS(G12C) mutant were

identified that shift the nucleotide preference of K-RAS(G12C) toward GDP and impair Raf activation[3]. In addition, synthetic α-helical peptides have been isolated that interfere with Sos-mediated nucleotide exchange on RAS and inhibit RAS function in cells[4,5].

We have taken a different approach to inhibit RAS through employing the monobody technology[6,7]. Monobodies are high affinity, synthetic proteins constructed based on the molecular scaffold of the fibronectin type III domain that often target functionally important sites of their respective target and thus can act as inhibitors[8].Unlike conventional antibodies, monobodies are insensitive to the redox potential of their environment and hence can be readily utilized as genetically encoded inhibitors[9]. High affinity monobodies have been isolated to a diverse array of targets including the extracellular domain of receptors, kinases, steroid hormone receptors, and modular protein domains[6,8]. Here, we report the isolation of a high affinity monobody, termed NS1, that selectively binds both H-RAS and K-RAS. NS1 potently inhibits H-RAS and K-RAS mediated signaling and transformation. Finally, biochemical and structural analyses reveal that NS1 inhibits RAS through binding a previously unrecognized interface important for dimerization/nanoclustering of RAS proteins. These findings reveal a novel approach to inhibit RAS-mediated signaling and transformation that is critical for RAS activation of RAF.

RESULTS

NS1 monobody selectively binds H-RAS and K-RAS

Given the challenges in pharmacologically inhibiting activated RAS[10], we hypothesized that there may exist functionally critical sites outside SW1 and SW2 that can be targeted for inhibition. To identify such sites, we generated monobodies specific for RAS. As a part of our ongoing investigation of H-RAS[11], we performed combinatorial library selection for monobodies that interacted with H-RAS in an unbiased manner with respect to their binding sites. We identified a monobody, termed NS1, that bound H-RAS with low nM affinity and K-RAS with slightly weaker affinity (Fig. 1a). Further, NS1 showed no detectable binding to N-RAS (Fig. 1a).

A series of cell-based experiments further supported the specificity and potency of NS1. Cyan fluorescent protein (CFP)-NS1 co-localized with YFP-tagged H-RAS and K-RAS, both on the plasma membrane and intracellular vesicles[12], but did not co-localize with YFP-N-RAS (Fig. 1b). In bimolecular fluorescence complementation (BiFC) assays, NS1 interacted equally well with wild type, constitutively activated and dominant negative H-RAS (Supplementary Results, Supplementary Fig. 1), suggesting that NS1 does not exhibit preference for the activation state of RAS, consistent with the *in vitro* binding profile (Fig. 1a). Finally, CFP-NS1, but not CFP alone, specifically captured H-RAS and to a lesser extent, K-RAS from cells, but did not capture N-RAS or the related RAS-like GTPase TC21/R-RAS2 (Fig. 1c). Thus, NS1 is specific to the H- and K-Ras members of the oncoprotein branch of the RAS subfamily[13].

NS1 monobody inhibits RAS-mediated signaling

When used as a genetically encoded, intracellular reagent, NS1 potently inhibited EGF activation of ERK-MAPK (Fig. 2a). NS1 attenuated ERK-MAPK activation by oncogenic H-RAS and K-RAS but not by oncogenic N-RAS, as anticipated from its binding specificity described above. Furthermore, NS1 did not inhibit signaling mediated by oncogenic BRAF or MEK1 (Fig. 2b and Supplementary Fig. 4a). The effect of NS1 on RAS-mediated signaling was not limited to ERK-MAPK activation; NS1 also inhibited AKT activation by oncogenic H-RAS and K-RAS but not by N-RAS (Fig. 2c and Supplementary Figs. 4b and 4c).

NS1 monobody inhibits RAS-mediated transformation

We next examined whether these effects of NS1 monobody on RAS-mediated signaling translated to comparable effects on RAS-mediated transformation. Consistent with the above molecular signaling analyses, NS1 inhibited transformation of cells by oncogenic HER2/Neu, H-RAS, and K-RAS but not N-RAS, BRAF, or MEK (Fig. 2d and Supplementary Fig. 5a). These results demonstrate that NS1 selectively inhibits signaling and oncogenic transformation by H-RAS and K-RAS but does not block the closely related family member, N-RAS, or oncogenic kinases downstream of RAS, *e.g.,* RAF and MEK.

Next, we examined the ability of NS1 to target oncogenic RAS in human tumor cells using an inducible expression system. Expression of NS1 as a CFP fusion protein, but not CFP alone, inhibited endogenous H-RAS(G12V)-mediated ERK activation and proliferation in bladder carcinoma cells (Fig. 2e and Supplementary Fig. 5b) but did not affect ERK activation or proliferation of melanoma cells harboring a mutant BRAF allele [BRAF(V600E)] (Fig. 2f). Thus, NS1 specifically inhibits endogenous mutant H-RAS but not downstream oncogenic kinases in human tumor cells.

NS1 does not affect nucleotide exchange on H-RAS

Because inhibitors of RAS-mediated signaling have been discovered that interfere with Sos-mediated nucleotide exchange[4,5,14] and prevent nucleotide loading[15], we tested whether NS1 might affect Sos-mediated nucleotide exchange. As anticipated from the observation that NS1 binding is insensitive to the nucleotide state of RAS (Fig. 1a), NS1 did not promote nucleotide release from H-RAS (Supplementary Fig. 7a) or block nucleotide exchange (Supplementary Fig 7b), thus excluding these modes of action for its inhibitory activity.

Structural basis of NS1-RAS interaction

To define the mechanism by which NS1 inhibits H-RAS mediated signaling, we determined a 1.4 Å-resolution crystal structure of NS1 in complex with GDP-loaded H-RAS (Supplementary Table 1). The structure revealed interaction of NS1 with the α4, β6, and α5 regions within the so-called allosteric lobe[16], which lie on the surface of RAS in opposition to SW1 and SW2 (Fig. 3a). This surface is also distinct from the RAS surface that binds a distal RAS-GTP activation site in Sos[17]. To our knowledge, no other RAS-interacting proteins have been reported to bind this surface. The interface is small for high-affinity protein interaction, with a buried surface area of 568 $Å^2$, but tightly packed with a shape complementarity value of 0.862. The H-RAS molecule maintained its conformation as

observed in published structures (Supplementary Fig. 8a). NMR chemical shift perturbation data (Fig. 3b) support the observed binding interface in solution. Furthermore, the lack of significant perturbations of HSQC resonances of H-RAS in the so-called effector lobe upon binding of NS1 to the allosteric lobe suggests that NS1 does not promote inter-lobe communication[16]. The FG loop of NS1, one of the loops that are diversified in the monobody library, forms two short β-strands that dock onto β6 of H-RAS and extend the central β-sheet of H-RAS (Supplementary Fig. 8b). In addition, NS1 utilizes predominantly aromatic side chains for interacting mainly with α4 of H-RAS (Supplementary Fig. 8c), as expected from our design of monobody combinatorial libraries[7].

NS1 makes extensive contacts with Arg135 of H-RAS, a residue identical in K-RAS but not N-RAS (Lys) (Fig. 3c). The Arg135 side chain forms a total of five polar interactions with surrounding residues (plus another with the water molecule) (Fig 3d). Tyr31 and Trp75 form a cage-like structure that restricts the conformation of Arg135 side chain, and there is also pi stacking between Tyr31 and Arg135. Based on this crystal structure, substitution of Arg135 with Lys as present in N-RAS would disrupt most of these contacts. Indeed, mutation of R135 to K or A in H-RAS(G12V) dramatically reduced NS1 binding rendering H-RAS resistant to NS inhibition (Fig. 3e and Supplementary Figs. 9a and 9b). These results confirm that Arg135 is a major specificity determinant and explains why NS1 does not bind or inhibit N-RAS (Figs. 1 and 2).

RAS crystal structures exhibit preferred dimer interface

To determine the relationship between NS1 binding and RAS inhibition, we systematically analyzed 113 available crystal structures of H-RAS (Fig. 4a). We consistently observed a specific dimer form, termed the α4-α5 dimer, in structures of H-RAS in the active state (as defined by the SW1 and SW2 conformations[18]) which was not present in inactive H-Ras structures (Fig. 4a and Supplementary Tables 2 & 3). This mode of dimerization existed across ten distinct crystal forms, suggesting that attainment of the α4-α5 dimer reflects an intrinsic property of active RAS and not an artefact of crystal packing. The α4-α5 dimer interface buries ~800Å^2 of surface area on RAS, a region distinct from and larger than that utilized by RAS to engage its effectors (~600Å^2). This dimer interface is distinct from surfaces utilized by RAS to bind GAPs[19] and GEFs[17,20]. The α4-α5 dimer state is compatible with RAS being anchored in the membrane and orients the effector binding region on both RAS protomers parallel to the plane of the membrane (Supplementary Fig. 9c), which would be necessary for productive RAS:effector interactions. Strikingly, NS1 binds at the center of this putative dimerization interface (Fig. 4b & c), thus precluding formation of the α4-α5 dimer in the presence of NS1. The α4-α5 dimer configuration is also present in the K-RAS(G12D) structure (PDB ID: 4EPR)[21] and overlaps a potential dimer interface identified in N-RAS by molecular modeling[22] and implicated in nanoclustering of RAS isoforms[23]. These observations suggest that this dimer configuration is conserved among RAS family members.

NS1 disrupts RAS dimerization/nanoclustering

Based on these observations, we hypothesized that NS1 inhibits oncogenic RAS-mediated signaling through blocking dimerization/nanoclustering of RAS thereby preventing RAF

activation (Fig. 5a). To directly test this hypothesis, we performed an electron microscopy (EM)-spatial analysis on RAS[24,25] (see Online Methods for detailed description). NS1 significantly reduced RAS nanoclustering which is quantified by the peak *L(r)-r* value, L_{max} (Fig. 5b, Supplementary Figs. 11a and 11b). Further analysis of the point patterns revealed that NS1 decreased the dimer/monomer ratio (Fig. 5c), as well as the population of multimers (Supplementary Figs. 11c and d), suggesting that NS1 disrupts RAS dimerization and subsequent nanoclustering. Consistent with these results, BRET analysis revealed that NS1 disrupted K-RAS but not N-RAS dimerization (Fig. 5d and Supplementary Fig. 11e). Thus, these findings suggest that NS1 disrupts dimerization/nanoclustering of both H- and K-RAS.

Residues within the α4-α5 interface, namely R135, D154 and R161, have been implicated in dimer formation[22]. However, charge-reversal mutations of these residues in the background of oncogenic H-RAS(G12V) did not affect ERK activation (Supplementary Figs. 9a, b and 12). These results indicate that these mutations are not sufficient to disrupt RAS signaling and suggest that these residues are not critical for RAS dimerization/nanoclustering.

The EM-spatial analysis also revealed that association of K-RAS, but not H-RAS, with the plasma membrane was reduced by NS1 expression (Fig. 5e). This observation is expected from the inhibition of dimerization by NS1. Each H-RAS molecule is firmly anchored by two palmitoyl chains and a farnesyl chain, but each K-RAS molecule is more weakly anchored by only a single farnesyl chain and a polybasic domain. Consequently, dimerization and oligomerization of K-RAS leads to substantially greater membrane binding avidity. NS1 binding reversed this process, resulting in dissociation of K-RAS. By contrast, each H-RAS molecule is firmly anchored by two palmitoyl chains and a farnesyl chain, rendering its membrane localization insensitve to the disruption of dimerization by NS1.

NS1 inhibits RAS-induced RAF activation

Recruitment and dimerization of RAF is a well established consequence of RAS activation[26,27]. To evaluate the ability of NS1 to alter effector binding and plasma membrane recruitment, we performed bivariate EM-co-clustering analyses[25,28,29]. NS1 significantly reduced co-localization of K-RAS(G12V), but not H-RAS(G12V), with CRAF at the plasma membrane (Supplementary Figs. 14a–c). Furthermore, NS1 reduced the number of gold-labeled RAF molecules on the plasma membrane in K-RAS(G12V), but not H-RAS(G12V) samples (Supplementary Fig. 14d). These results are consistent with earlier work showing that K-RAS is more efficient at recruiting and retaining CRAF on the plasma membrane than H-RAS[29,30]. Similar results were obtained by co-immunoprecipitation of oncogenic H- or K-RAS with RAF (Fig. 6a and Supplementary Fig. 16a) or binding to the RAF RBD (Supplementary Figs. 16b and c). In addition, NS1 did not affect binding of GTP loaded H-$RAS_{1–166}$ to GST-RAF RBD *in vitro* (Supplementary Fig. 16d). Further, BRET analysis revealed that NS1 disrupts CRAF interaction with K-RAS(G12V) but not N-RAS(G12V) (Supplementary Figs. 18 and 19). Thus, NS1 prevents dimerization and subsequent nanoclustering of oncogenic H-RAS and K-RAS at the plasma membrane resulting in decreased engagement of RAF by K-RAS but not H-RAS. As would be predicted, NS1

inhibits oncogenic H- and K-RAS-induced CRAF:BRAF heterodimerization (Figs. 6b, c, and Supplementary Fig. 19)[26,27] and subsequent RAF activation (Fig. 6d, Supplementary Fig. 21).

DISCUSSION

Development of effective RAS inhibitors represents a holy grail in cancer biology[10]. Our discovery of a potent monobody inhibitor that binds a region distinct from inhibitors that directly impair effector interactions with the switch regions[3,31–33] represents a novel strategy to inhibit oncogenic RAS-mediated signaling and transformation. Our multi-disciplinary study has substantially increased the support for the importance of the α4-α5 interface for RAS dimerization/nanoclustering, signaling and oncogenic transformation.

Although inhibition of kinase dimerization is a common theme in blocking signaling by RTKs[34] and the RAF-MAPK pathway[26,35], the role of dimerization in RAS function remains a point of significant debate. Radiation inactivation studies suggest that both wild type and mutationally activated RAS function in an oligomeric state[36]. Chemical dimerization of RAS induces RAF activation[37] and recent super resolution microscopy studies support the premise that RAS proteins form dimers[38] to promote RAF dimerization[37,39] and activation[26]. Finally, EM-spatial mapping studies indicate that RAS proteins function in small, transient nanoclusters consisting of ~6–7 RAS proteins[24] that lead to RAF recruitment and activation. While these data support the premise that RAS dimerizes in the cellular context, clear demonstration of RAS dimerization has been enigmatic. A missing piece of this puzzle has been a tool to directly modulate RAS dimerization. Our results now establish that binding of NS1 to the α4-α5 interface of RAS reduces RAS dimerization/nanoclustering and prevents effector activation, suggesting that RAS dimerization is a requisite step in signal transmission.

In contrast to the characterization of full-length RAS in the cellular context, there are conflicting reports of whether the G domain of RAS forms dimers in solution[40,41]. This dimerization interaction is certainly weak, as the G domain is predominantly monomeric in solution even at high protein concentrations. However, RAS dimers are observed at extremely high protein concentrations such as in crystal structures (Fig. 4A and Supplementary Tables 2 & 3)[22]. These seemingly conflicting observations can be reconciled by the fact that tethering of RAS to the plasma membrane through its C-terminal lipid modifications reduces the dimensionality and thus increases the effective local concentration of RAS, increasing the probability of dimer formation[38]. The detection of RAS dimers in the cellular context may also be facilitated by RAF that has an intrinsic property to dimerize[26]. Nevertheless, our results with NS1 monobody clearly demonstrate the importance of the α4-α5 interface for RAS-induced dimerization of RAF.

The α4-α5 interface has been proposed as a dimerization interface in RAS proteins, with specific residues contributing to the formation of the proposed dimer[22]. However, mutation of several of these residues (namely R135, D154 and R161)[22] did not affect oncogenic H-RAS-mediated activation of ERK (Supplementary Figs. 9a, b and 12). This difference between perturbation by point mutations and by the NS1 monobody is intriguing and indeed

provides mechanistic insights into the nature of RAS dimerization/nanoclustering. Our results suggest that individual RAS protomers may not need to physically interact through a single, specific mode of protein-protein interaction. Rather, upon GTP binding, the α4-α5 regions of RAS may reorient in close proximity to promote RAF dimerization and activation. Binding of NS1 to the α4-α5 interface would provide significant steric interference to this clustering thereby preventing RAS-induced effector dimerization, whereas a mutation may not. Alternatively, NS1 binding may alter the orientation of RAS with the plasma membrane thereby inducing an autoinhibited conformation[42]. Further studies combining multiple biophysical techniques will define the atomic details of RAS dimer/nanocluster.

Our results with NS1 monobody also highlight differences between H-RAS and K-RAS in terms of their localization at the plasma membrane and their engagement of RAF. Although NS1 has a roughly 5-fold higher affinity for H-RAS vs K-RAS, engagement of NS1 reduced the amount of K-RAS at the plasma membrane and the recruitment of RAF while the amount of H-RAS at the plasma membrane and the H-RAS:RAF interaction remained relatively refractory to NS1 binding. Several possibilities may explain these differences. The displacement of K-RAS from the plasma membrane upon binding NS1 may result in decreased engagement of RAF. Furthermore, NS1 may promote differing degrees of membrane occlusion of the effector binding region in K-RAS vs H-RAS due to differences in their orientational equilibrium[42]. Such an effect may be different for H-RAS and K-RAS because their distinct C-terminal modifications may result in differences in the dynamic interaction with the membrane. In addition, RAS proteins exhibit intramolecular communication between the allosteric and effector lobes[16]. While our structural analyses suggest that NS1 does not promote significant inter-lobe communication in H-RAS, K-RAS could exhibit more significant conformational perturbations upon NS1 binding resulting in allosteric changes in the effector domain. Nevertheless, it is clear that for both H-RAS and K-RAS, NS1 engagement of the α4-α5 interface inhibited RAS-induced RAF dimerization and activation. Future studies will determine the precise molecular explanation for these differences and the possibility of exploiting them for selective targeting of RAS isoforms.

Online Methods

Cell culture, subcloning, transfections and reagents

COS, HEK293, HEK293T and NIH3T3 cells have been in Dr. O'Bryan's laboratory for more than 17 years. NIH-3T3 cells are a common model cell line to examine *in vitro* oncogenic transformation by oncogenes such as RAS, RAF, etc. COS, HEK-293T, and HEK-293 cells represent model heterologous systems for performing biochemical analyses. HEK-293, HEK-293T and COS1 cells were cultured in DMEM with 10% FBS. NIH-3T3 cells were cultured in DMEM with 10% calf serum. T24 human bladder carcinoma cells (ATCC) were cultured in McCoy's 5A with 10% FBS. A375 human melanoma cells (kindly provided by Dr. Andrew Aplin) were grown in DMEM with 10% FBS. All growth media were commercially purchased (Corning). HEK-293, HEK-293T, COS1 and NIH-3T3 cells were transiently transfected using empirically determined concentrations of polyethyleneimine (PEI) along with Opti-Mem reduced serum media (Life Technologies) and serum-free

DMEM. NS1 was PCR amplified from the monobody vector using primers: 5'CTCGAGACTACAAAGACGATGACGACAAGGGATCCGTTTCTTCTGTTCCGACCA A3' and 5'CTCGAGTCAGGTACGGTAGTTAATCGA3', digested with XhoI and cloned into the XhoI site of the cyan fluorescent protein tagged, pECFP-C1 and the BiFC vector VC-155 for mammalian cell expression. pTRIPz-CFP (control) and pTRIPz-CFP-NS1 vectors were generated by modification of the original pTRIPz vector (Thermo Scientific Open Biosystems). pTRIPz was digested with AgeI and MluI to remove both tRFP and the shRNAmir sequences. PCR amplified CFP or CFP-NS1 fragments from the pECF-C1 vector were cloned into pTRIPz using In-Fusion Cloning (Clontech) following manufacturers instructions.

Antibodies

The following antibodies were purchased from commercial sources: ERK1/2 1:2000 dilution (Cat. 9102S), phospho-ERK1/2 1:2000 dilution (Cat. 9101L), MEK1/2 1:1000 dilution (Cat. 9126S), phospho-MEK1/2 (Ser217/221) 1:1000 dilution (Cat. 9121S), AKT 1:4000 dilution (Cat. 9272S), phospho-AKT (S473) 1:1000 dilution (Cat. 9271S) and phospho-AKT (T308) 1:1000 dilution (Cat. 9275S) were all purchased from Cell Signaling Technology; FLAG-M2 monoclonal antibody 1:4000 dilution (Cat. F3165-1MG) and anti-FLAG polyclonal antibody 1:2000 dilution (Cat. F7425-.2MG) were purchased from Sigma Aldrich; anti-HA.11 monoclonal antibody 1:4000 dilution (Cat. 16B12) and anti-HA.11 polyclonal antibody (Cat. Poly9023) were purchased from Biolegend; anti-Myc 1:2000 dilution (EMD Millipore Cat. 05-724); anti-CRAF 1:1000 (BD Biosciences, Cat. 610151); anti-GST (Z-5) 1:5000 dilution (Santa Cruz Biotechnology, Cat. sc-459); anti-GFP 1:4000 (Clontech, Cat. 632381); anti-pan-RAS 1:1000 dilution (ABCAM Cat. ab108602); and anti-pan-RAS (LA069) 1:1000 dilution (Quality Biotechnology Inc.).

Generation of stable lines

HEK-293T cells were used to generate lentivirus for infection of T24 cells. These packaging cells were PEI transfected using 20 μg of either pTRIPz-CFP or pTRIPz-CFP-NS1 along with a plasmid encoding the pMD2.G the viral envelope and pCMVdR8.74 to generate viral particles. The following day packaging cells were placed in fresh media and cells were seeded for infection. On day 2 post-transfection, conditioned media from the HEK-293T cells were collected, filtered, and used to infect cells followed by selection in 750 ng/ml puromycin. Following selection colonies were pooled to generate a polyclonal cell line, which was used for all subsequent analyses.

Protein expression and purification

Bacterially expressed GST fusion proteins and H-RAS have been previously described[11]. H-RAS (Uniprot: P01116, residues 1–166, and residues 1–174), K-RAS (Uniprot:P01116, isoform 2B, residues 1–174), N-RAS (Uniprot: P01111, residues 1–174) and NS1 monobody were prepared as a fusion C-terminal to His_6, a biotin-acceptor tag, and a TEV cleavage site using an in-house vector termed pHBT[9]. Mutations were introduced using the method of Kunkel et al.[43]. The proteins were produced in *E. coli* BL21(DE3) containing the pBirAcm plasmid (Avidity) in the presence of 50 μM D-biotin for *in vivo* biotinylation. They were purified using Ni-Sepharose columns (GE-Healthcare). Their purity and

monomeric state were confirmed using a Superdex 75 size-exclusion column (GE Healthcare) and mass spectroscopy. For crystallization, the proteins were expressed in BL21(DE3) without the addition of biotin in the media, purified as described above and the affinity tags for each protein were removed using the tobacco etch virus (TEV) protease. The cleaved tag and uncleaved protein were removed by passing the sample through a Ni-Sepharose column.

Monobody generation and characterization

Given our prior interests in understanding the function of different nucleotide bound states of H-RAS[11], we initially sought to isolate high affinity reagents to different nucleotide states of this GTPase. For monobody selection, biotinylated H-RAS (residues 1–166) was used. For testing isoform specificity, biotinylated RAS samples containing residues 1–174 were used, because the G-domain of K-RAS extends beyond residue 166. The biotinylated H-RAS protein bound to GDP or GTPγS was prepared by incubating the H-RAS sample prepared from E. coli with 1 mM GDP or GTPγS in 20 mM Tris-HCl buffer pH 7.5 containing 15 mM EDTA, 5 mM $MgCl_2$ and 1 mM DTT for 30 min at 30°C followed by an addition of $MgCl_2$ at a final concentration of 20 mM and incubation on ice for 5 min. The apo H-RAS protein was prepared by the same way except that no nucleotide was added.

General methods for phage- and yeast-display library sorting and gene shuffling have been described[7,8]. The NS1 monobody was isolated from the "side-and-loop" combinatorial library constructed in the phage display format[7] as follows. We performed three separate selections using H-RAS apo, H-RAS/GDP and H-RAS/GTPγS in parallel. Four rounds of phage-display selection were performed in the TBS/Mg/BSA/TCEP buffer (50 mM TrisCl, 150 mM NaCl, pH7.5, 20 mM $MgCl_2$, 5 mg/ml BSA, 0.2 mM TCEP), using protein concentrations of 100, 100, 50 and 50 nM for the first through fourth rounds. In each round, phage clones that bound to the target were captured using streptavidin-coated magnetic beads and amplified. The monobody genes from the enriched clones were amplified using PCR and the segments encoding to the N- and C-terminal halves of the monobodies were recombined and assembled, as detailed previously[7]. This “gene-shuffled” pool of monobody genes were used to transform yeast EBY100 to construct a library in the yeast display format. Two rounds of yeast-display library sorting were performed using 100 and 50 nM protein concentrations, as described using a FACS Aria sorter (BD Biosciences). Individual clones were grown and tested for binding to H-RAS/GTPγS and H-RAS/GDP. The NS1 monobody was recovered from all three selection campaigns.

Quantitative binding measurements in the yeast display format were performed using a Millipore Guava flow cytometer as described previously[7,8]. Individual clones from sorted libraries were isolated on agar plates and grown in liquid media. Approximately 100,000 yeast cells for each clone were incubated with various concentrations of biotinylated target in BSS/Mg/TCEP buffer for H-RAS/GDP and H-RAS/GTPγS, and in BTE/TCEP buffer [20mM TrisCl (pH7.5), 15mM EDTA, 1mg/ml BSA, 0.2mM DTT] for H-RAS apo at room temperature for 30 min with shaking. The yeast cells were washed and stained with neutravidin-Dylight 650 conjugate (Thermo Fisher Scientific) in the wells of a 96-well filter plate (MultiScreenHTS HV, 0.45 μm pore size; Millipore). The stained cells were analyzed

using a Guava EasyCyte 6/L flow cytometer (Millipore). The K_D values were determined from plots of the mean fluorescence intensity versus target concentration by fitting the 1:1 binding model using the KaleidaGraph program (Synergy Software). We have validated using numerous monobodies that K_D values measured in this manner are consistent with those determined from biophysical methods using purified monobodies[7,9,44].

Crystallization, diffraction data collection and structure determination

The NS1 and H-RASGDP proteins were mixed in a 1:1 molar ratio, and the complex was purified using a Superdex 75 column. The complex was concentrated to a total protein concentration of 16 mg/mL in 10mM Tris-Cl buffer pH 8.0 containing 50 mM NaCl, 20 mM $MgCl_2$ and 0.5 mM TCEP. Crystals were obtained in 0.2M ammonium fluoride, 20% PEG 3350, pH 6.2, at 19 °C by the hanging-drop vapor diffusion method. Crystals were frozen in a mixture of 75% mother liquor and 25% ethylene glycol. X-ray diffraction data were collected at the X-ray Operations and Research beamline 19-BM-D at the Advanced Photon Source, Argonne National Laboratory at a wavelength of 0.979 Å and at 100 K. Data collection information is reported in Supplementary Table 1. Diffraction data were processed and scaled with the HKL-3000 package[45]. The NS1/H-RAS166 structure was determined by molecular replacement in Phaser[46]. A multicopy search was performed using an H-RASGDP Structure (PDB ID: 4Q21) and a monobody structure excluding the loop regions (PDB ID: 4JE4). Manual model building, solvent addition, and refinement of the structure was conducted iteratively using Coot[47] and phenix.refine[48]. Model validation was conducted using the Molprobity server[49] as well as the Protein Data Bank validation server. The final structural model was of good geometry, with 98.4% of residues in favored regions and 1.6% in allowed regions of the Ramachandran analysis. Molecular graphics were generated using PyMOL[50]. Surface area calculations were performed using the PROTORP protein–protein interaction server[51]. Shape complementarity was determined using the Sc statistic[52].

Cell signaling assays

ERK and AKT activation assays were measured by transfecting HEK293 cells with MYC-ERK or HA-AKT constructs along with the indicated expression constructs. Following immunopurification of the tagged kinase, samples were analyzed for activation of ERK/AKT by Western blot with phosphospecific antibodies. Activation was quantified by densitometry using ImageJ. Quantification of kinase activation was determined by dividing the level of phosphokinase by that of total kinase and normalizing to unstimulated, vector control sample. Experiments were performed in triplicate. RAS activation was determined essentially as previously described[53]. HEK 293 cells were transiently transfected with the indicated constructs, serum starved overnight in DMEM alone and stimulated with EGF (100 ng/ml for 10 min) where indicated. Oncogene transfected cells were not stimulated with growth factor. Cells were then lysed in GTPase buffer containing (25 mM HEPES, 150 mM NaCl, 10% glycerol, 1% Triton X-100, 25 mM $MgCl_2$, 1 mM EDTA, 25 mM NaF, 0.25% DOC, pH 7.5) and incubated at 4 °C for 1 hour with either GST or GST-RAF RBD. Precipitated HA-H-RAS was examined by Western blot and quantified by densitometry using ImageJ. Relative RAS activity was determined by dividing precipitated HA-H-RAS by the total HA-H-RAS in whole cell lysates. Interaction of RAS-family GTPases with NS1 in cells was measured by co-immunoprecipitation. Briefly, HEK-293 cells were transfected

with the indicated constructs. Following immunoprecipitation of CFP or CFP-NS1, samples were analyzed by Western blot using the indicated antibodies for co-precipItation of the indicated HA-tagged GTPases. RAS interaction with RAF was also measured by co-immunoprecipitation. Briefly, T24 cells stably transfected with pTRIPz constructs encoding with CFP or CFP-NS1 were induced to express for 48 hours with 2 μg/ml doxycycline. Following immunoprecipitation of endogenous RAS, samples were analyzed by Western blot for co-precipitation of CRAF, BRAF, and monobody. Experiments were performed in triplicate. RAF activation was measured essentially as described[54]. Briefly, HEK-293 cells were transfected with the indicated constructs. Following immunopurification of endogenous CRAF, samples were incubated with purified kinase-dead MEK1 in an *in vitro* kinase reaction containing: 20 mM Tris (pH 7.4), 20 mM NaCl, 1 mM DTT, 10 mM $MgCl_2$, 1 mM $MnCl_2$ and 20 μM ATP for 30 minutes at 30°C with constant shaking. Reactions were terminated by addition of boiling hot sample buffer and then analyzed by Western blot using a phosphospecific MEK antibody (Cell Signaling).

Bimolecular fluorescence complementation

Expression constructs consisting of the FLAG-tagged N-terminus or HA-tagged C-terminus of Venus (VN and VC, respectively) were kindly provided by Chang-Deng Hu. All H-RAS and NS1 cDNA sequences were cloned into these vectors such that the Venus fragments were fused to the N-terminus of the respective protein. COS1 cells were transiently transfected late in the day and then imaged the following morning. CFP was co-transfected along with the BiFC constructs, but at a five fold-lower amount, to mark transfected cells.

Cell viability assays

T24 or A375 cells (1000 per well) were plated on 24-well plates in complete media (McCoy's 5A with 10% FBS plus 0.75 μg/ml puromycin and 2 μg/ml doxycycline to induce expression from the pTRIPz constructs) for the indicated number of days. On the indicated day, media was removed and replaced with 100 μl of serum-free McCoy's 5A, cells were harvested after 30 minutes at 37°C. Viability was assayed using CellTiter Glow (Promega). Luminescence was quantified on a Dynex 96-well microtiter plate luminometer according to the manufacture's instructions.

Transformation assays

NIH 3T3 cells were seeded in 60 mm dishes to a density of 2.5×10^5 cells in complete media. Cells were transfected with indicated constructs. Media changes were performed every 3 days. Foci were counted and stained after 14 – 21 days. All assays were performed in triplicate and repeated three times with the exception of NeuT which was only performed twice.

Identification of H-RAS α4-α5 dimeric assemblies in the Protein Data Bank

The α4-α5 H-RAS dimeric structure (Protein Data Bank, PDB ID 5p21[55]) was used as a template. The PISA server[56] was utilized to search the entire PDB for all H-RAS structures in which i) the α4-α5 dimer conformation was found, and ii) in which the α4-α5 dimer was not found. The 39 structures in which the specific dimer was not found were further

analyzed in PyMol[50] to manually compare the tertiary structure to determine its active state based on the conformation of switch regions[18] as superimposed on the active state PDB ID 5P21.

BRET assays

HEK293T cells were maintained in DMEM supplemented with 10% FBS and Penicillin/Streptomycin. For titration curves, 1.5×10^5 HEK293T cells were seeded in 12-well plates and transfected the next day with polyethylenimine (PEI)[57]. Forty-eight hours post-transfection, cells were washed, resuspended in HBSS buffer (Wisent) and transferred to white opaque 96-well microtiter plates (Greiner). BRET measurements were done as follows. BRET signals and luciferase activity were read 15 minutes post-addition of 2.5 μM Coelenterazine 400a (Biotium) using a Victor plate reader (Perkin Elmer) equipped with BRET2 emission filter set (donor: 400nm ± 20 nm; acceptor: 510 nm ± 20 nm). BRET signals correspond to the light emitted by the GFP10 acceptor constructs (510 nm ± 20 nm) upon addition of Coelenterazine 400a divided by the light emitted by the RlucII donor constructs (400 nm ± 20 nm). Total GFP10 or mCherry levels were separately detected on a FlexStation II (Molecular Devices) with excitation and emission peaks set at 400 and 510 nm, and 580 and 635 nm, respectively. Total intrinsic GFP10 (expressed as Relative Fluorescence Units; RFU) and RlucII (Relative Luminescence Units; RLU) signals were used as proxies to ensure that similar protein expression was obtained across conditions (Supplementary Figs. 18 and 19). For more detailed BRET procedures, see Lavoie et al. 2013 Supplementary Note 1[57].

Nucleotide exchange assays

Nucleotide release was measured essentially as described[17]. H-RAS was purified from bacteria and buffer exchanged with PD-10 columns (GE Healthcare) into nucleotide loading buffer (20 mM Tris-HCl, 50 mM NaCl, 4 mM EDTA, 1 mM DTT, pH 7.5) and loaded with MANT-GTP (Life Technologies). Unincorporated MANT-GTP was removed and MANT-GTP-loaded H-RAS was exchanged into reaction buffer (40 mM HEPES-KOH, 10 mM $MgCl_2$, 1 mM DTT, pH 7.5) using NAP-5 columns (GE Healthcare). Reactions were initialized by addition of the indicated proteins. Nucleotide incorporation was measured essentially as described[58]. H-RAS was exchanged into reaction buffer (20 mM TRIS-HCl, 50 mM NaCl, 10 mM MgCl2, 1 mM DTT, pH 7.5) using NAP-5 columns. H-RAS was preincubated with NS1 for 10 minutes where indicated. Reactions were initialized by addition of 400 nM MANT-GTP and SOScat (where indicated). All nucleotide exchange assays were performed at room temperature for 1800 seconds. Fluorescence was excited at 355 nm, and emission was monitored at 460 nm using a FlexStation™II (Molecular Devices Corporation) 96-well plate reader.

Monobody competition for RAS-RAF interaction

Bacterial expressed H-RAS was incubated in Loading Buffer (20 mM Tris-HCl, pH 7.6, 15 mM EDTA, 5 mM $MgCl_2$, 1 mM DTT, 0.1 mM PMSF, 10% glycerol) with either 1mM GTPγS or 1mM GDP for 30 minutes at 30°C. The reaction was quenched with 65mM $MgCl_2$ and kept on ice for 10 minutes. After nucleotide loading, 250 nM HRAS was incubated with 125 nM, 250 nM, or 1.25 uM of NS1 for 15 mins at 4°C followed by

addition of 850nM of GST-RAF RBD or GST. Reactions were incubated for 1 hr at 4°C. Beads were then washed 3× with Washing Buffer (10 mM Tris-HCl, pH 7.6, 5 mM $MgCl_2$, 10% glycerol, 1 mM DTT, 0.1% TritonX-100, 0.1 mM PMSF) and run on an SDS-PAGE gel to visualize bound proteins by Coomassie staining.

EM-Spatial Mapping

To directly test the effect of NS1 on RAS dimerization/nanoclustering, we co-expressed GFP-tagged K-RAS(G12V) with RFP empty vector or RFP-NS1 in baby hamster kidney (BHK) cells and performed an EM-spatial analysis which has been described in detail elsewhere[24,59,60]. Briefly, the apical plasma membrane of BHK cells transiently expressing GFP-tagged RAS proteins, along with RFP empty vector or RFP-NS1, was attached to copper EM grids. After fixation with 4% paraformaldehyde (PFA) and 0.1% glutaraldehyde, GFP-RAS on the plasma membrane was immuno-labeled with 4.5nm gold nanoparticles pre-coupled to anti-GFP antibody, which was then embedded in uranyl acetate. Gold particle distribution was visualized by transmission EM (TEM) imaging using JEOL JEM-1400 transmission EM. ImageJ was then used to assign×and y coordinates of gold particles in a 1-μm^2 area on intact and featureless plasma membrane sheets. Ripley's K-function was used to calculate the gold particle distribution and the extent of nanoclustering[24,59]:

$$K(r)=An^{-2}\sum_{i\neq j} w_{ij}1(\|x_i - x_j\| \leq r) \quad \text{(Eq. A)}$$

$$L(r) - r = \sqrt{\frac{K(r)}{\pi}} - r \quad \text{(Eq. B)}$$

where $K(r)$ is the univariate K-function for a distribution of n points in a selected plasma membrane area A and indicates the extent of nanoclustering; r = length scale with a range of $1 < r < 240$ nm at 1-nm increments; $\|\cdot\|$ is Euclidean distance; indicator function of $1(\cdot)$ has a value of 1 if $\|x_i - x_j\| \leq r$ and a value of 0 otherwise; and w_{ij}^{-1} describes the circumferential fraction of the circle with center x_i and radius $\|x_i - x_j\|$ within area A. An unbiased edge correction was included for points at the edge of the study area. Monte Carlo simulations then estimated a 99% confidence interval (99% C.I.), which was used to normalize $K(r)$ to yield $L(r) - r$. The extent of nanoclustering is quantified by the peak $L(r) - r$ value, L_{max}. The model tests the null hypothesis that a completely random distribution of gold particles yields a $L(r) - r$ value of 0 for all values of r. At least 15 PM sheets were imaged, analyzed and pooled for each condition. Statistical significance between different conditions was evaluated against 1000 bootstrap samples, which were constructed exactly as described[29].

EM-Spatial Mapping-Bivariate K-function analysis

The bivariate K-function analyzes co-clustering/co-localization between RAS and CRAF on the plasma membrane inner leaflet. BHK cells were co-transfected with GFP-RAS and RFP-CRAF, along with GST empty vector or GST-NS1. Apical plasma membrane was attached

and fixed to copper EM grids, which were then immuno-labeled with both 2nm gold coupled to anti-RFP antibody and 6nm gold coupled to anti-GFP antibody. Followed by EM imaging, x and y coordinates of both population of gold particles were assigned using ImageJ. Co-distribution between 6nm and 2nm gold populations was analyzed using a bivariate K-function. (Eqs. C–F):

$$K_{\mathrm{biv}}(r)=(n_b+n_s)^{-1}[n_bK_{sb}(r)+n_sK_{bs}(r)] \quad \text{(Eq. C)}$$

$$K_{bs}(r)=\frac{A}{n_bn_s}\sum_{i=1}^{n_b}\sum_{j=1}^{n_s}w_{ij}1(\|x_i-x_j\|\le r) \quad \text{(Eq. D)}$$

$$K_{sb}(r)=\frac{A}{n_bn_s}\sum_{i=1}^{n_s}\sum_{j=1}^{n_b}w_{ij}1(\|x_i-x_j\|\le r) \quad \text{(Eq. E)}$$

$$L_{\mathrm{biv}}(r)-r=\sqrt{\frac{K_{\mathrm{biv}}(r)}{\pi}}-r \quad \text{(Eq. F)}$$

where the bivariate estimator, $K_{biv}(r)$, consists of two individual bivariate K-functions: $K_{bs}(r)$ estimates the spatial distribution of 6nm (big, assigned as "*b*") gold particles with respect to each 2nm (small, assigned as "*s*") gold particle whereas $K_{sb}(r)$ quantifies the distribution of the small gold particles around each big gold particle. A selected plasma membrane sheet area A contains n_b, number of 6-nm gold particles and n_s, number of 2-nm small gold particles. Other symbols are the same as described in Eqs.A and B. Monte Carlo simulations then estimated the 95% confidence interval (95% C.I.), which was used to normalize $K_{biv}(r)$ to yield $L_{biv}(r)$-r which evaluates the co-clustering at the length scale r. Here, we aim to test the null hypothesis that complete spatial segregation between big and small gold populations yields a $L_{biv}(r)$-r value of 0 for all values of r. Positive deviation above the 95% C.I. indicates statistically meaningful co-localization between GFP-RAS and RFP-CRAF. We then calculated the area-under-the-curve for each $L_{biv}(r)$-r curve over a fixed range $10 < r < 110$ nm to yield the bivariate $L_{biv}(r)$-r integrated (or LBI) to quantify the extent of co-localization or co-clustering between RAS and CRAF:

$$LBI=\int_{10}^{110}\mathrm{Std}L_{\mathrm{biv}}(r)-r.dr \quad \text{(Eq. G)}$$

At least 15 PM sheets were imaged, analyzed and pooled for each condition. Data are presented as mean ± *s.e.m.* Bivariate statistical significance between conditions was

evaluated via comparing against 1000 bootstrap samples, which was constructed exactly as described[60].

Supplementary Material

Refer to Web version on PubMed Central for supplementary material.

Acknowledgments

We wish to thank J. Kuriyan and Y. Kondo for the purified Sos protein; S. Campbell for the K-RAS expression construct; A. Cox for the N-RAS(G12D) construct; W. Hahn for the pBabe-Puro-MEK-DD (Addgene plasmid # 15268); G. Clark for pCGN-Raf; B. Kreutz for valuable assistance with the fluorescent nucleotide exchange assays; D. Morrison for purified MEK (K97R). R.S.S is supported by an NIH F31 Predoctoral Award (CA192822). This work was supported in part by a CIHR award to F.Sicheri (FDN 143277); a Merit Review Award (1I01BX002095) from the United States (U.S.) Department of Veterans Affairs Biomedical Laboratory Research and Development Service to J.P.O. and NIH awards to J.P.O (CA116708 and CA201717) and S.K. (GM090324); a Catalyst award from the Chicago Biomedical Consortium with support from the Searles Funds at The Chicago Community Trust (S.K. and J.P.O.). This research used resources of the Advanced Photon Source, a U.S. Department of Energy (DOE) Office of Science User Facility operated for the DOE Office of Science by Argonne National Laboratory under Contract No. DE-AC02-06CH11357. The contents do not represent the views of the U.S. Department of Veterans Affairs or the United States Government.

S.K. and A.K. are inventors on a patent application filed by the University of Chicago that covers a design of monobody libraries (US 13/813,409). S.K., A.K. and J.P.O. are inventors on a patent application jointly filed by the University of Chicago and University of Illinois that covers the NS1 monobody.

References

1. Karnoub AE, Weinberg RA. Ras oncogenes: split personalities. Nat Rev Mol Cell Biol. 2008; 9:517–531. [PubMed: 18568040]
2. Cox AD, Der CJ. Ras history: The saga continues. Small GTPases. 2010; 1:2–27. [PubMed: 21686117]
3. Ostrem JM, Peters U, Sos ML, Wells JA, Shokat KM. K-Ras(G12C) inhibitors allosterically control GTP affinity and effector interactions. Nature. 2013; 503:548–551. [PubMed: 24256730]
4. Leshchiner ES, et al. Direct inhibition of oncogenic KRAS by hydrocarbon-stapled SOS1 helices. Proc Natl Acad Sci U S A. 2015; 112:1761–1766. [PubMed: 25624485]
5. Patgiri A, Yadav KK, Arora PS, Bar-Sagi D. An orthosteric inhibitor of the Ras-Sos interaction. Nat Chem Biol. 2011; 7:585–587. [PubMed: 21765406]
6. Koide A, Bailey CW, Huang X, Koide S. The fibronectin type III domain as a scaffold for novel binding proteins. J Mol Biol. 1998; 284:1141–1151. [PubMed: 9837732]
7. Koide A, Wojcik J, Gilbreth RN, Hoey RJ, Koide S. Teaching an old scaffold new tricks: monobodies constructed using alternative surfaces of the FN3 scaffold. J Mol Biol. 2012; 415:393–405. [PubMed: 22198408]
8. Koide S, Koide A, Lipovsek D. Target-binding proteins based on the 10th human fibronectin type III domain ((1)Fn3). Methods Enzymol. 2012; 503:135–156. [PubMed: 22230568]
9. Sha F, et al. Dissection of the BCR-ABL signaling network using highly specific monobody inhibitors to the SHP2 SH2 domains. Proc Natl Acad Sci U S A. 2013; 110:14924–14929. [PubMed: 23980151]
10. Cox AD, Fesik SW, Kimmelman AC, Luo J, Der CJ. Drugging the undruggable RAS: Mission possible? Nat Rev Drug Discov. 2014; 13:828–851. [PubMed: 25323927]
11. Wong KA, et al. A new dimension to Ras function: a novel role for nucleotide-free Ras in Class II phosphatidylinositol 3-kinase beta (PI3K-C2b) regulation. PLoS ONE. 2012; 7:e45360. [PubMed: 23028960]
12. Chiu VK, et al. Ras signalling on the endoplasmic reticulum and the Golgi. Nat Cell Biol. 2002; 4:343–350. [PubMed: 11988737]

13. Colicelli J. Human RAS superfamily proteins and related GTPases. Sci STKE. 2004; 2004:RE13. [PubMed: 15367757]
14. Burns MC, et al. Approach for targeting Ras with small molecules that activate SOS-mediated nucleotide exchange. Proc Natl Acad Sci U S A. 2014; 111:3401–3406. [PubMed: 24550516]
15. Feramisco JR, et al. Transient reversion of ras oncogene-induced cell transformation by antibodies specific for amino acid 12 of ras protein. Nature. 1985; 314:639–642. [PubMed: 2581140]
16. Fetics SK, et al. Allosteric effects of the oncogenic RasQ61L mutant on Raf-RBD. Structure. 2015; 23:505–516. [PubMed: 25684575]
17. Margarit SM, et al. Structural evidence for feedback activation by Ras. GTP of the Ras-specific nucleotide exchange factor SOS. Cell. 2003; 112:685–695. [PubMed: 12628188]
18. Hall BE, Bar-Sagi D, Nassar N. The structural basis for the transition from Ras-GTP to Ras-GDP. Proc Natl Acad Sci U S A. 2002; 99:12138–12142. [PubMed: 12213964]
19. Scheffzek K, et al. The Ras-RasGAP complex: structural basis for GTPase activation and its loss in oncogenic Ras mutants. Science. 1997; 277:333–338. [PubMed: 9219684]
20. Boriack-Sjodin PA, Margarit SM, Bar-Sagi D, Kuriyan J. The structural basis of the activation of Ras by Sos. Nature. 1998; 394:337–343. [PubMed: 9690470]
21. Sun Q, et al. Discovery of small molecules that bind to K-Ras and inhibit Sos-mediated activation. Angew Chem Int Ed Engl. 2012; 51:6140–6143. [PubMed: 22566140]
22. Guldenhaupt J, et al. N-Ras forms dimers at POPC membranes. Biophys J. 2012; 103:1585–1593. [PubMed: 23062351]
23. Abankwa D, et al. A novel switch region regulates H-ras membrane orientation and signal output. EMBO J. 2008; 27:727–735. [PubMed: 18273062]
24. Plowman SJ, Muncke C, Parton RG, Hancock JF. H-ras, K-ras, and inner plasma membrane raft proteins operate in nanoclusters with differential dependence on the actin cytoskeleton. Proc Natl Acad Sci U S A. 2005; 102:15500–15505. [PubMed: 16223883]
25. Zhou Y, et al. SIGNAL TRANSDUCTION. Membrane potential modulates plasma membrane phospholipid dynamics and K-Ras signaling. Science. 2015; 349:873–876. [PubMed: 26293964]
26. Rajakulendran T, Sahmi M, Lefrancois M, Sicheri F, Therrien M. A dimerization-dependent mechanism drives RAF catalytic activation. Nature. 2009; 461:542–545. [PubMed: 19727074]
27. Freeman AK, Ritt DA, Morrison DK. Effects of Raf dimerization and its inhibition on normal and disease-associated Raf signaling. Mol Cell. 2013; 49:751–758. [PubMed: 23352452]
28. Zhou Y, et al. Signal integration by lipid-mediated spatial cross talk between Ras nanoclusters. Mol Cell Biol. 2014; 34:862–876. [PubMed: 24366544]
29. Plowman SJ, Ariotti N, Goodall A, Parton RG, Hancock JF. Electrostatic interactions positively regulate K-Ras nanocluster formation and function. Mol Cell Biol. 2008; 28:4377–4385. [PubMed: 18458061]
30. Yan J, Roy S, Apolloni A, Lane A, Hancock JF. Ras isoforms vary in their ability to activate Raf-1 and phosphoinositide 3-kinase. J Biol Chem. 1998; 273:24052–24056. [PubMed: 9727023]
31. Lim SM, et al. Therapeutic targeting of oncogenic K-Ras by a covalent catalytic site inhibitor. Angew Chem Int Ed Engl. 2014; 53:199–204. [PubMed: 24259466]
32. Shima F, et al. In silico discovery of small-molecule Ras inhibitors that display antitumor activity by blocking the Ras-effector interaction. Proc Natl Acad Sci U S A. 2013; 110:8182–8187. [PubMed: 23630290]
33. Wu X, Upadhyaya P, Villalona-Calero MA, Briesewitz R, Pei D. Inhibition of Ras-Effector Interaction by Cyclic Peptides. Medchemcomm. 2013; 4:378–382. [PubMed: 23585920]
34. Zhang X, et al. Inhibition of the EGF receptor by binding of MIG6 to an activating kinase domain interface. Nature. 2007; 450:741–744. [PubMed: 18046415]
35. Herrero A, et al. Small Molecule Inhibition of ERK Dimerization Prevents Tumorigenesis by RAS-ERK Pathway Oncogenes. Cancer Cell. 2015; 28:170–182. [PubMed: 26267534]
36. Santos E, Nebreda AR, Bryan T, Kempner ES. Oligomeric structure of p21 ras proteins as determined by radiation inactivation. J Biol Chem. 1988; 263:9853–9858. [PubMed: 3133369]
37. Inouye K, Mizutani S, Koide H, Kaziro Y. Formation of the Ras dimer is essential for Raf-1 activation. J Biol Chem. 2000; 275:3737–3740. [PubMed: 10660519]

38. Nan X, et al. Ras-GTP dimers activate the Mitogen-Activated Protein Kinase (MAPK) pathway. Proc Natl Acad Sci U S A. 2015; 112:7996–8001. [PubMed: 26080442]
39. Nan X, et al. Single-molecule superresolution imaging allows quantitative analysis of RAF multimer formation and signaling. Proc Natl Acad Sci U S A. 2013; 110:18519–18524. [PubMed: 24158481]
40. Muratcioglu S, et al. GTP-Dependent K-Ras Dimerization. Structure. 2015; 23:1325–1335. [PubMed: 26051715]
41. Kovrigina EA, Galiakhmetov AR, Kovrigin EL. The Ras G Domain Lacks the Intrinsic Propensity to Form Dimers. Biophys J. 2015; 109:1000–1008. [PubMed: 26331257]
42. Mazhab-Jafari MT, et al. Oncogenic and RASopathy-associated K-RAS mutations relieve membrane-dependent occlusion of the effector-binding site. Proc Natl Acad Sci U S A. 2015

Online References

43. Kunkel TA, Roberts JD, Zakour RA. Rapid and efficient site-specific mutagenesis without phenotypic selection. Methods Enzymol. 1987; 154:367–382. [PubMed: 3323813]
44. Gilbreth RN, et al. Isoform-specific monobody inhibitors of small ubiquitin-related modifiers engineered using structure-guided library design. Proc Natl Acad Sci U S A. 2011; 108:7751–7756. [PubMed: 21518904]
45. Minor W, Cymborowski M, Otwinowski Z, Chruszcz M. HKL-3000: the integration of data reduction and structure solution--from diffraction images to an initial model in minutes. Acta Crystallogr D Biol Crystallogr. 2006; 62:859–866. [PubMed: 16855301]
46. McCoy AJ, et al. Phaser crystallographic software. J Appl Crystallogr. 2007; 40:658–674. [PubMed: 19461840]
47. Emsley P, Cowtan K. Coot: model-building tools for molecular graphics. Acta Crystallogr D Biol Crystallogr. 2004; 60:2126–2132. [PubMed: 15572765]
48. Adams PD, et al. PHENIX: a comprehensive Python-based system for macromolecular structure solution. Acta Crystallogr D Biol Crystallogr. 2010; 66:213–221. [PubMed: 20124702]
49. Chen VB, et al. MolProbity: all-atom structure validation for macromolecular crystallography. Acta Crystallogr D Biol Crystallogr. 2010; 66:12–21. [PubMed: 20057044]
50. DeLano, W. The PyMol Molecular Graphics System. Schrödinger, LLC; (www.pymol.org)
51. Reynolds C, Damerell D, Jones S. ProtorP: a protein-protein interaction analysis server. Bioinformatics. 2009; 25:413–414. [PubMed: 19001476]
52. Lawrence MC, Colman PM. Shape complementarity at protein/protein interfaces. J Mol Biol. 1993; 234:946–950. [PubMed: 8263940]
53. Taylor SJ, Resnick RJ, Shalloway D. Nonradioactive determination of Ras-GTP levels using activated ras interaction assay. Methods Enzymol. 2001; 333:333–342. [PubMed: 11400349]
54. Bondzi C, Grant S, Krystal GW. A novel assay for the measurement of Raf-1 kinase activity. Oncogene. 2000; 19:5030–5033. [PubMed: 11042690]
55. Pai EF, et al. Refined crystal structure of the triphosphate conformation of H-ras p21 at 1.35 A resolution: implications for the mechanism of GTP hydrolysis. Embo J. 1990; 9:2351–2359. [PubMed: 2196171]
56. Krissinel E, Henrick K. Inference of macromolecular assemblies from crystalline state. J Mol Biol. 2007; 372:774–797. [PubMed: 17681537]
57. Lavoie H, et al. Inhibitors that stabilize a closed RAF kinase domain conformation induce dimerization. Nat Chem Biol. 2013; 9:428–436. [PubMed: 23685672]
58. Abe K, et al. Vav2 is an activator of Cdc42, Rac1, and RhoA. J Biol Chem. 2000; 275:10141–10149. [PubMed: 10744696]
59. Prior IA, Muncke C, Parton RG, Hancock JF. Direct visualization of Ras proteins in spatially distinct cell surface microdomains. J Cell Biol. 2003; 160:165–170. [PubMed: 12527752]
60. Prior IA, Parton RG, Hancock JF. Observing cell surface signaling domains using electron microscopy. Sci STKE. 2003; 2003:PL9. [PubMed: 12684529]

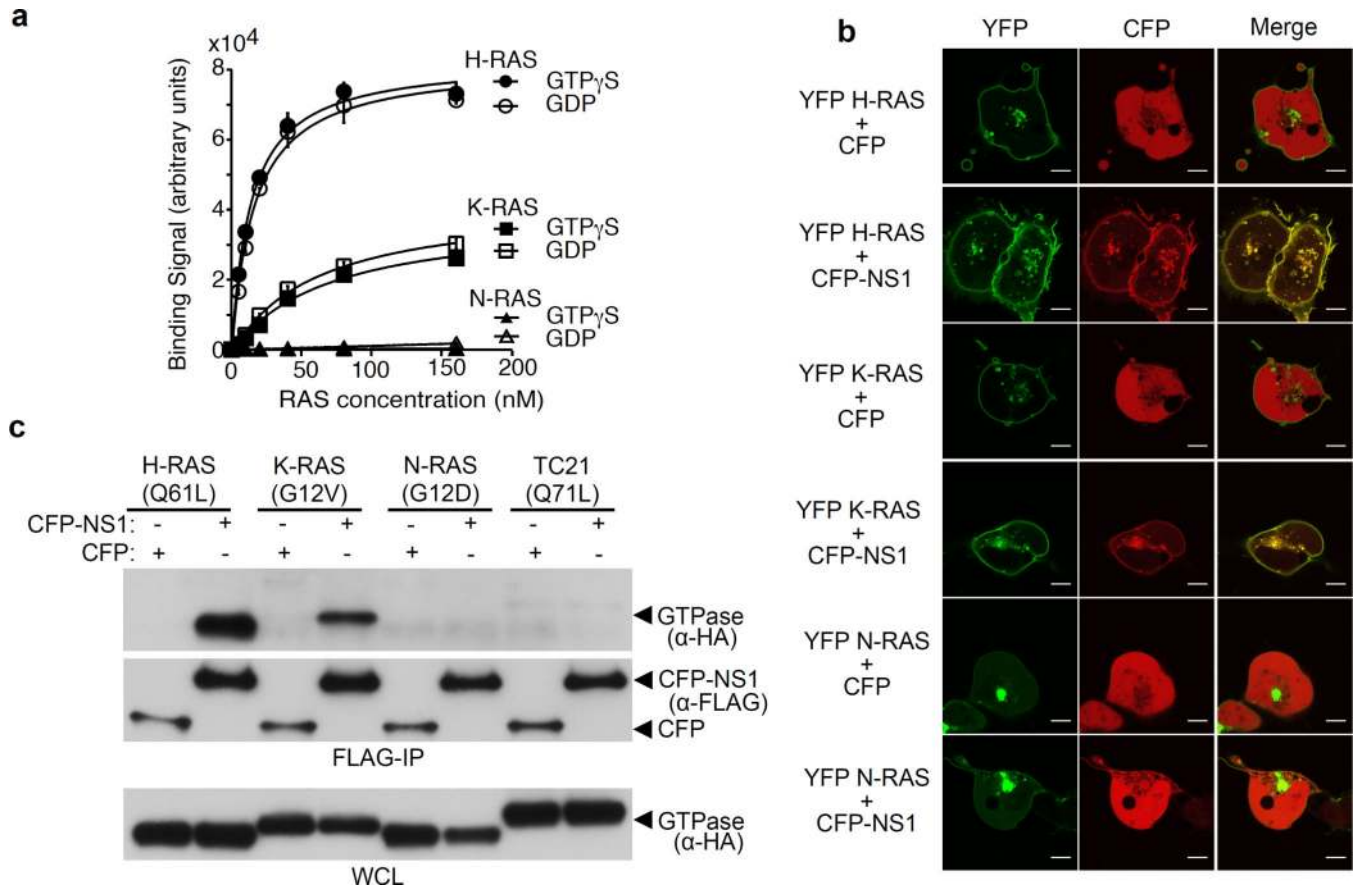

Figure 1. RAS-specific monobody targets H-RAS and K-Ras

a, Binding titration of NS1 displayed on yeast cells with the RAS isoforms bound to nucleotide using flow cytometry detection. Affinity values (K_D) are as follows: H-RAS GTPγS, 13.5±1.9 nM; H-RAS GDP, 15.7±2.7 nM; K-RAS GTPγS, 67±16 nM; K-RAS GDP, 60±11 nM; N-RAS GTPγS, not detectable; N-RAS GDP, not detectable. Error bars represent s.d. from N=3. The errors for the K_D values are s.d. from three independent measurements. **b & c**, Assessment of NS1 specificity in cells. **b,** Co-localization of CFP-NS1 (pseudo-colored red) co-localizes with YFP-tagged RAS isoforms (each pseudo-colored green). Scale bars, 10 um. **c,** Co-immunoprecipation of HA-tagged RAS isoforms by CFP-NS1. Full blot images for Fig. 1c are shown in Supplementary Fig. 2

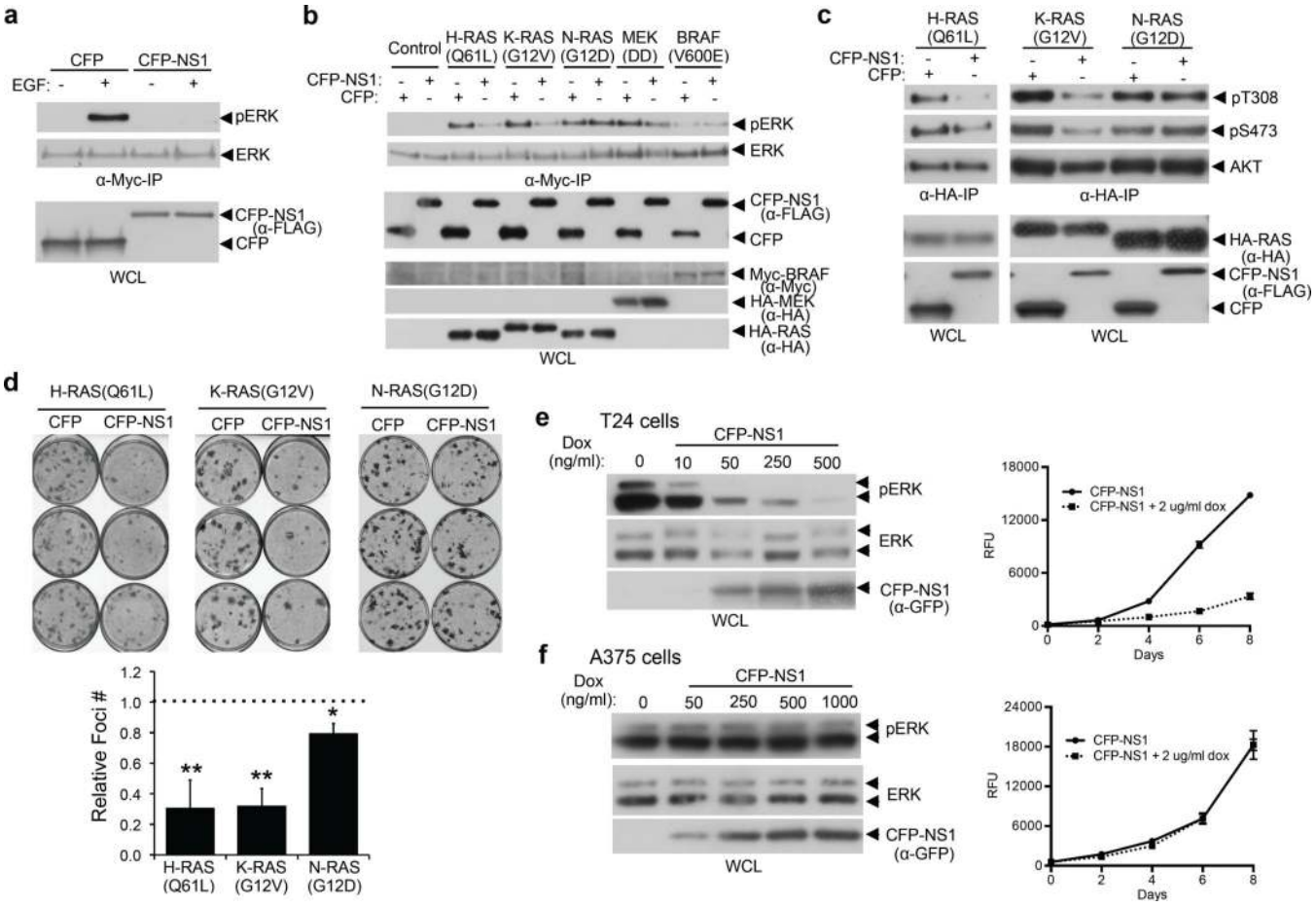

Figure 2. NS1 inhibits RAS-mediated signaling and transformation

a, Effect of CFP-NS1 expression on EGF-stimulated ERK activation in HEK293 cells. CFP-NS1 and MYC-tagged ERK were co-expressed, and phosphorylation of MYC-tagged ERK was detected by Western blot with phosphospecific ERK antibodies. **b,** Cells transfected with the indicated oncogene along with CFP or CFP-NS1 were analyzed for ERK activation as in **a**. **c,** Effect of NS1 on AKT activation by RAS. Cells were transfected and analyzed as in **b** except HA-AKT was used in place of MYC-ERK. Quantification of results from **b** and **c** is provided in Supplementary Fig. 4. **d,** NIH/3T3 transformation assay. Quantification of relative foci number for each oncogene is shown in the graphs. Results represent the ratio of foci number in presence of CFP-NS1 vs CFP alone and are the average of three independent experiments performed in triplicate +/− *s.d.* p values were determined by a Student's t-test between CFP and CFP-NS1 for each oncogene. **, p<0.01, *, p<0.05. Effects of NS1 on oncogenic HER2/Neu, BRAF, and MEKK1 are shown in Supplementary Fig. 5a. **e** & **f**. Effects of NS1 on signaling and proliferation of human tumor cells. **e**. Titration of CFP-NS1 effects on ERK activation and proliferation (graph) in T24 bladder carcinoma cells (**e**) and A375 melanoma cells (**f**). Results in the graphs are the average of triplicate wells +/− *s.e.m.* shown by bars. Western blots in **e** and **f** are representative of at least 3 independent experiments. Full blot images for Figs 2a–c, e and f and Supplementary Fig. 5b are shown in Supplementary Figs. 3 and 6, respectively.

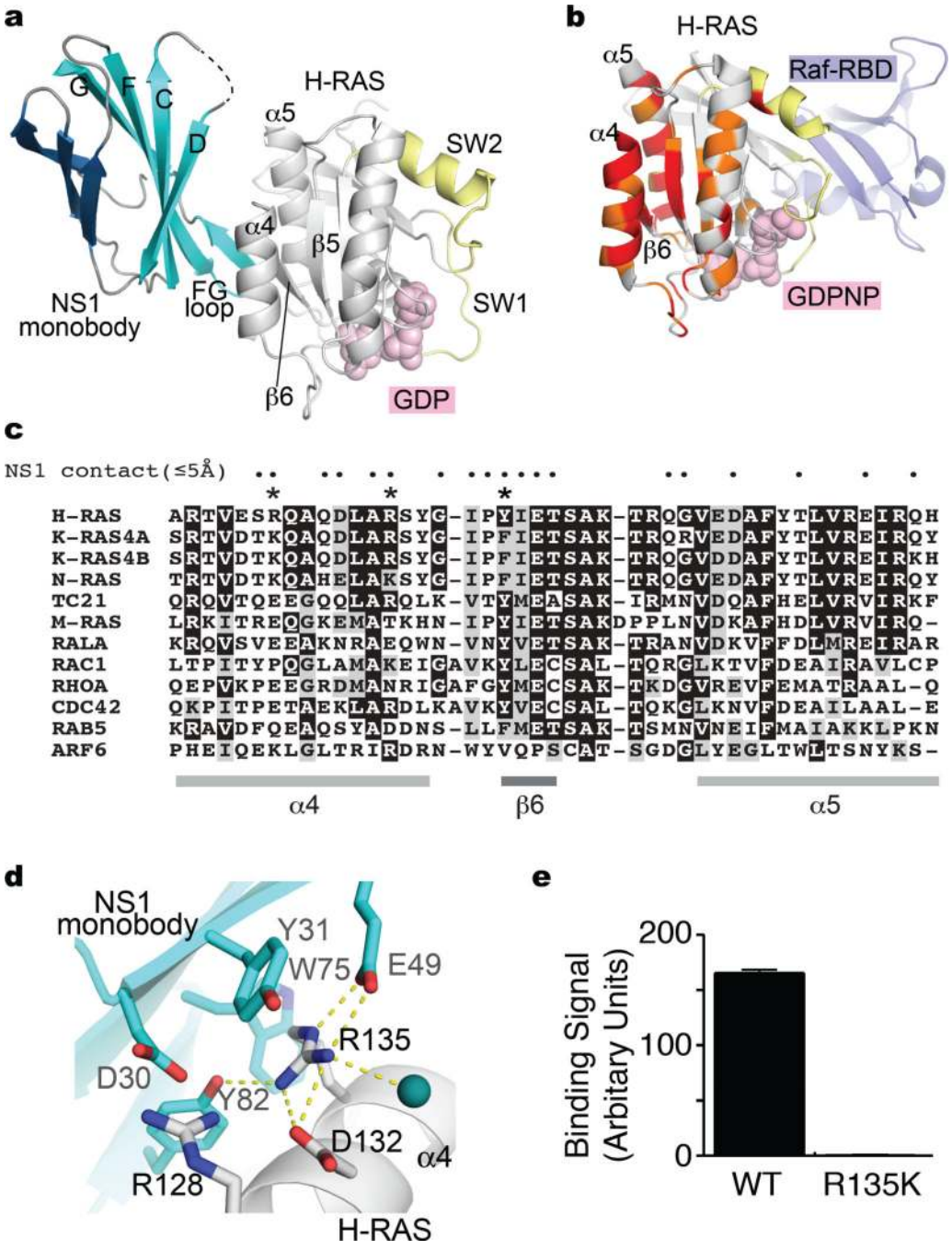

Figure 3. NS1 targets the α4-α5 interface in RAS distal to switch regions

a, Crystal structure of NS1:H-RAS-GDP. **b**, Chemical shift changes in H-RAS upon NS1 binding. Amino acids undergoing strong chemical shifts are highlighted red and weaker reacting residues highlighted orange in the H-RAS:RAF RBD structure (PDB ID: 4G0N). The most significant changes occurred in the β5, α4, β6, and α5 regions of H-RAS, which lie on the surface of RAS in opposition to the switch regions which bind effectors such as RAF, indicated in the figure. **c,** Amino acid sequences of the α4-β6-α5 region (residues 122–166) of the RAS isoforms. Asterisks mark amino acids whose mutation affects affinity

to NS1. Dots mark amino acid side chains within 5 angstroms of amino acid side chains in NS1. **d,** Recognition of R135 in H-RAS by NS1. Polar interactions between R135 and surrounding amino acids and water (green sphere) are highlighted by dashed yellow lines. **e.** Effect of Arg135 to Lys mutation on H-RAS binding NS1 *in vitro*. Results are the average of three independent binding experiments +/− *s.d.* WT, 165.3 +/−2.9 AU; R135K, 0.44+/−0.29 AU.

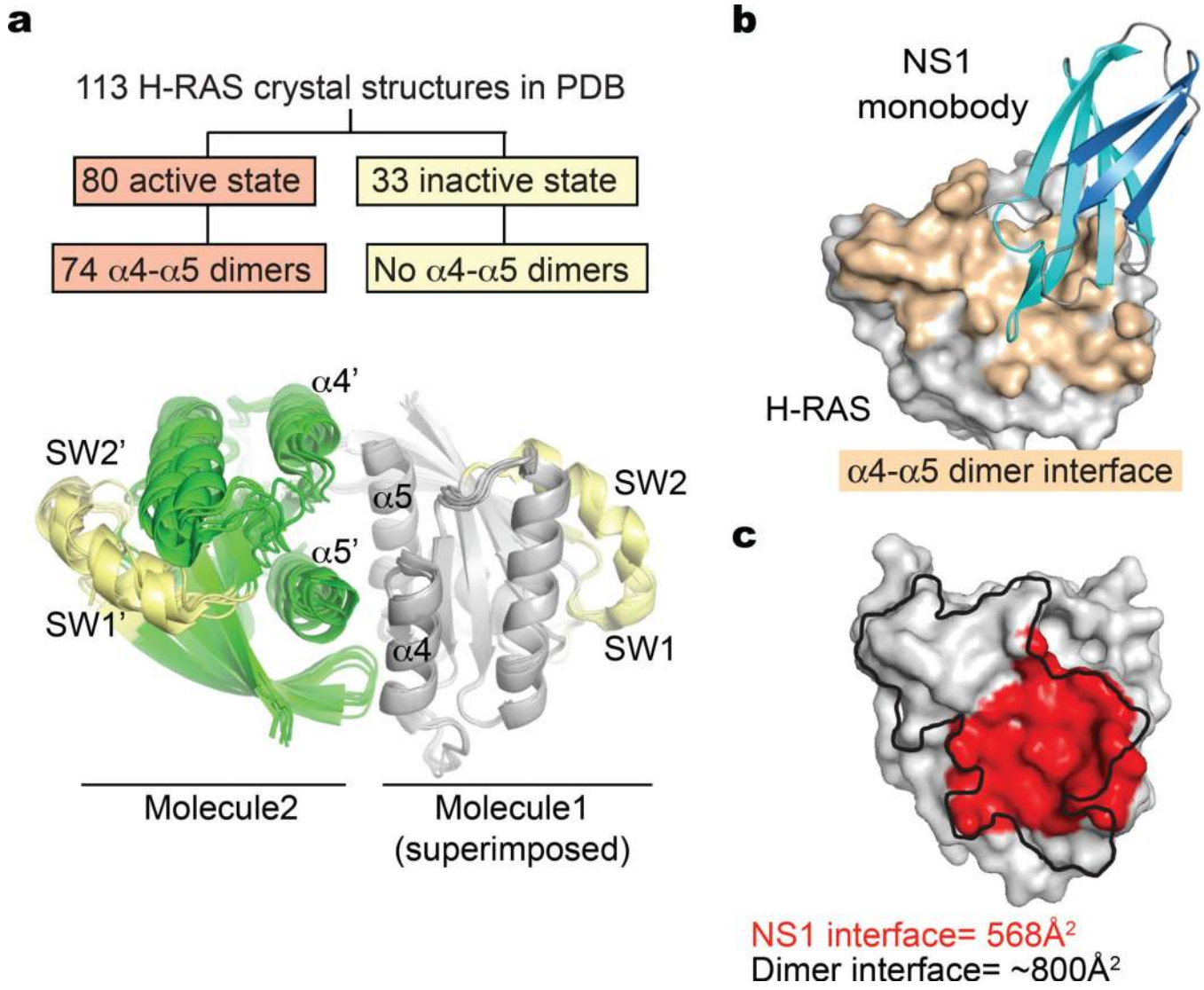

Figure 4. NS1 targets a putative RAS dimerization interface

a, Comparison of H-RAS crystal structures in the Protein Data Bank (PDB). Seventy-four of 80 active state H-RAS structures contained α4-α5 dimers but no α4-α5 dimers were present in inactive state structures. A protomer (shown in gray) of the α4-α5 dimers from six active state H-RAS structures (PDB ID, 5P21, 1AGP, 4L9W, 2C5I, 3K9L, and 3KUD) were superimposed using Pymol. SW1 and SW2 regions are highlighted yellow. **b,** NS1 monobody binds the α4-α5 dimer interface as highlighted in brown. The dimer interface shown is from PDB ID: 5P21. These regions overlap with the presumed dimerization interface identified in N-RAS[22]. **c.** Comparison of NS1 binding surface (highlighted red) and α4-α5 dimer interface (denoted with black boarder) on H-RAS structure.

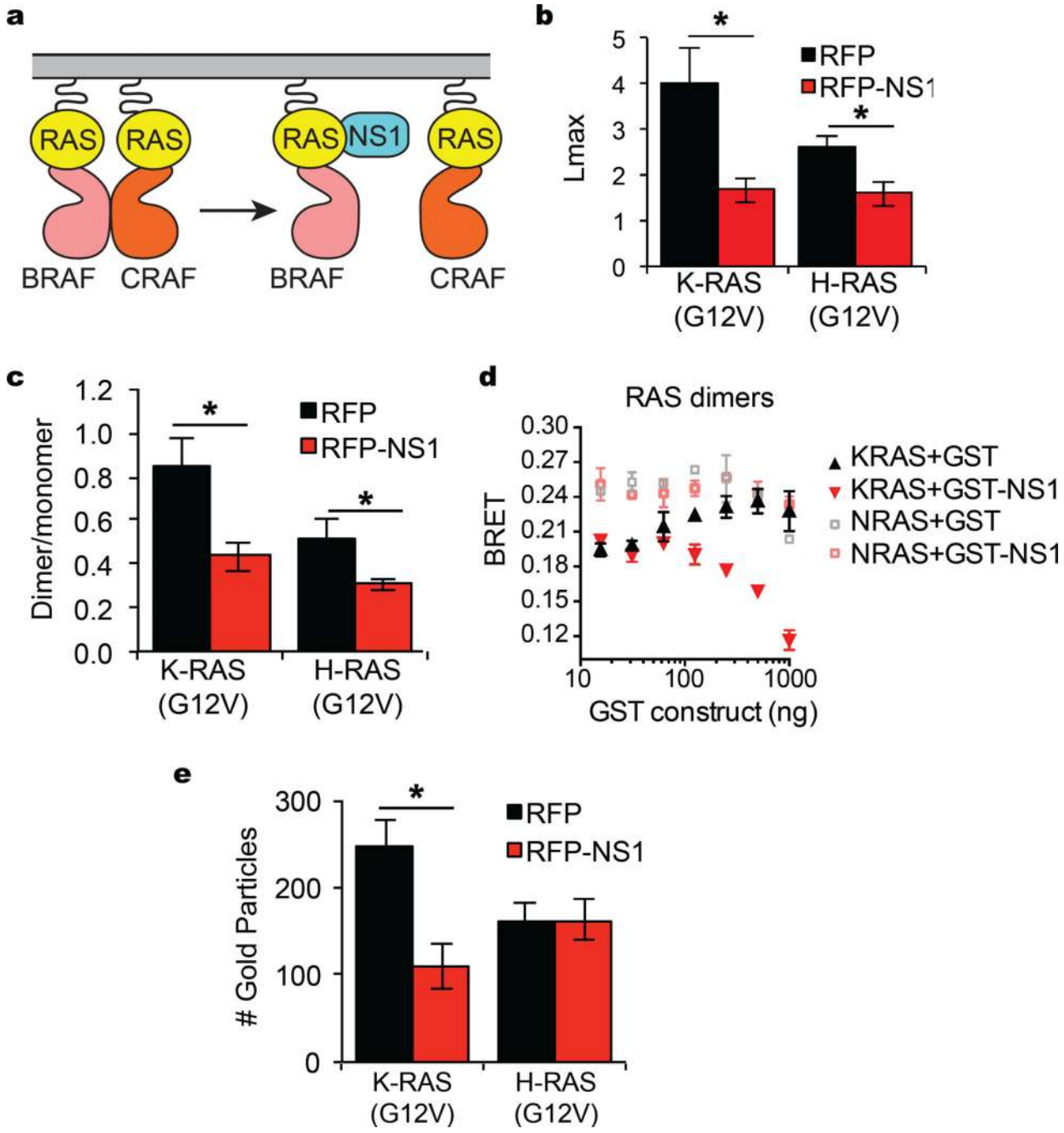

Figure 5. NS1 blocks RAS dimerization/nanoclustering and subsequent RAF activation

a, Model for NS1 inhibition of RAS-mediated signaling. **b**, The extent of nanoclustering of GFP-H-RAS(G12V) or GFP-K-RAS(G12V) in BHK plasma membrane sheets immunolabeled with α-GFP-4.5nm gold gold particles was evaluated in K-functions summarized as L_{max}. Data represent mean L_{max} values ± *s.e.m.* (Number of samples analyzed: H-RAS+RFP, n=19; H-RAS+RFP-NS1, n=23; K-RAS+RFP, n=16; K-RAS+RFP-NS1, n=24.; * indicates $p < 0.05$, bootstrap tests). **c**, The dimer/monomer ratio estimated from data in **b**. Analysis of the point patterns from **b** allowed calculation of dimer/monomer

ratio shown as mean ± *s.e.m.* (The number of samples analyzed was the same as in **b**; * indicates $p < 0.05$, one-way ANOVA). **d**, Effect of NS1 on K-RAS(G12V) or N-RAS(G12V) dimerization measured by BRET. Each experiment was performed at least three times with values representing the average of three independent transfections +/− *s.d.* Additional controls for these experiments are provided in Supplementary Fig. 11e. **e,** Plasma membrane localization of GFP-K-RAS(G12V) and GFP-H-RAS(G12V) determined by counting total number of gold-labelled GFP particles per $1\mu m^2$ area of intact plasma membrane sheets. Values are shown as mean ± *s.e.m.* ($n>15$; * indicates $p < 0.05$, one-way ANOVA).

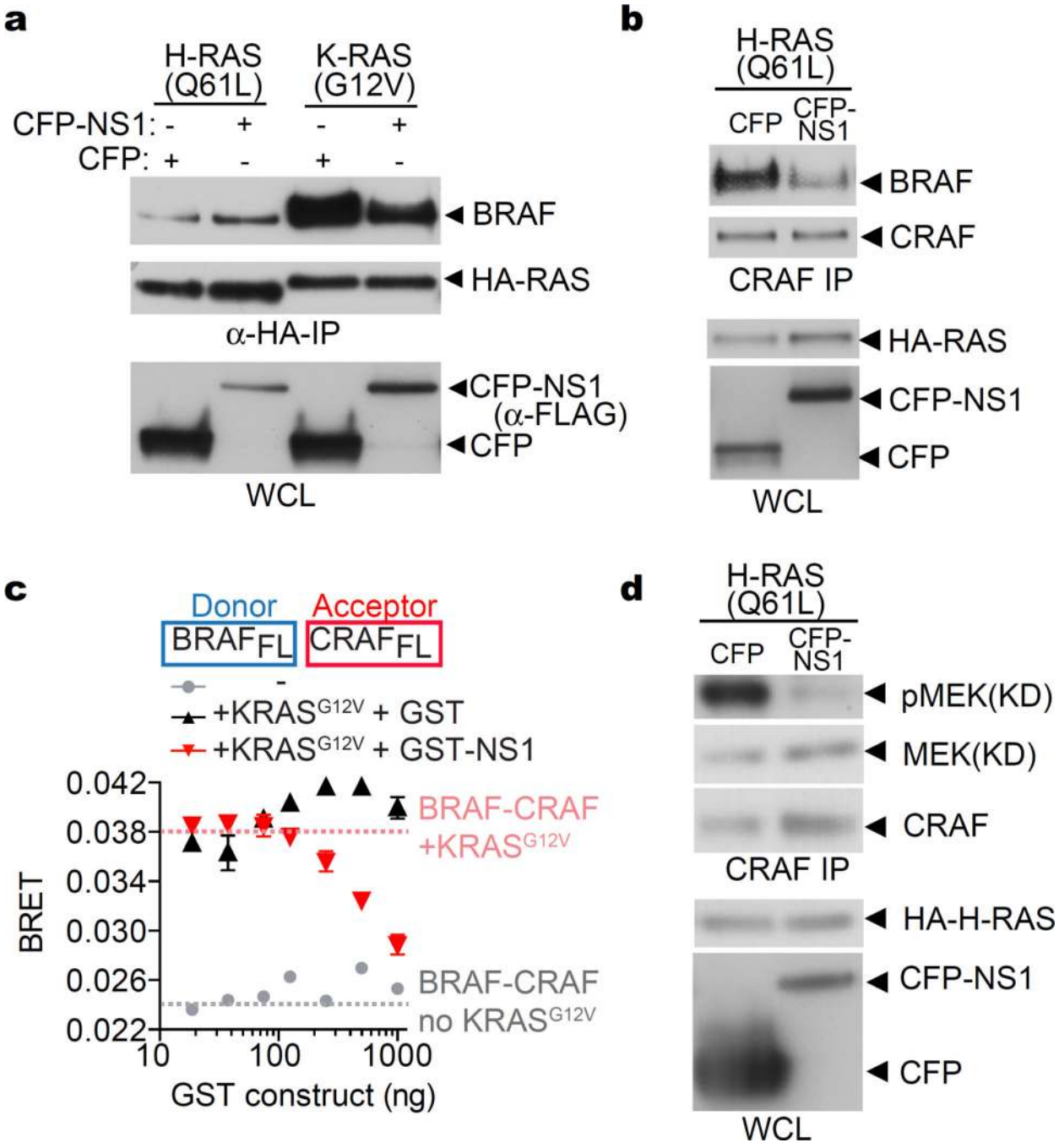

Figure 6. Effect of NS1 on oncogenic RAS activation of RAF

a, Effect of CFP-NS1 vs CFP on binding of endogenous BRAF to either H-RAS(G12V) or K-RAS(G12V). Results are representative of at least 3 independent experiments. **b,** Effects of CFP-NS1 vs CFP on oncogenic H-RAS(Q61L)-induced heterodimerization of CRAF and BRAF measured by co-immunoprecipitation in HEK-293T cells. **c,** K-RAS(G12V) induced heterodimerization of BRAF and CRAF measured by BRET. Each experiment was performed at least three times with values representing the average of three independent transfections +/− *s.d.* Additional controls are provided in Supplementary Fig. 19. **d,** Effect of

NS1 on *in vitro* RAF kinase activity. Quantification of results from three independent experiments is shown in Supplementary Fig. 21. Full blot images for Figs 6a, b, and d are shown in Supplementary Fig. 15.